

The Pennsylvania State University
The Graduate School
Department of Mechanical and Nuclear Engineering

**DESIGN, FABRICATION, AND TESTING OF A
PIEZOELECTRIC T-BEAM ACTUATOR**

A Thesis in
Mechanical Engineering

by

Andrew D. Hirsh

© 2008 Andrew D. Hirsh

Submitted in Partial Fulfillment
of the Requirements
for the Degree of

Master of Science

December 2008

The thesis of Andrew D. Hirsh was reviewed and approved* by the following:

Christopher D. Rahn
Professor of Mechanical Engineering
Thesis Co-Advisor

Srinivas A. Tadigadapa
Associate Professor of Electrical Engineering
Thesis Co-Advisor

Gary H. Koopmann, P.E.
Distinguished Professor of Mechanical Engineering

Karen A. Thole
Professor of Mechanical Engineering
Head of the Department of Mechanical and Nuclear Engineering

*Signatures are on file in the Graduate School

ABSTRACT

This thesis introduces a novel T-beam actuator fabricated using a precision dicing saw. Bulk PZT is diced to produce cantilevered beams with T-shaped cross sections. Electrodes are deposited on the top of the web, bottom of the flange, and the top of the right and left flanges. Selectively activating these electrodes creates active and passive regions in the PZT structure and in-plane and out-of-plane bending with bimorph-like performance. Several devices are fabricated and experimentally tested for in-plane and out-of-plane displacement using a microscope/camera with optical measurement. Combinations of applied voltage, ground, and float on the four electrodes are tested to determine optimal actuation cases that maximize tip deflection. For 19 mm long and 1 mm thick T-beam actuators, 15 microns of out-of-plane deflection amplitude and 5.5 microns of in-plane deflection amplitude is achieved at 0.4 V/micron actuation voltage.

TABLE OF CONTENTS

LIST OF FIGURES	v
LIST OF TABLES.....	vii
ACKNOWLEDGEMENTS.....	viii
Chapter 1 Introduction.....	1
Chapter 2 T-Beam Concept	3
Chapter 3 Actuator Design & Device Fabrication.....	5
3.1 Actuator Design.....	5
3.2 Device Fabrication.....	7
Chapter 4 Experimental Setup and Testing	11
4.1 Experimental Setup.....	11
4.2 Device Characteristics	12
4.3 Device Testing.....	13
4.4 Results and Discussion	21
Chapter 5 Conclusions & Future Work	23
Bibliography	25
Appendix A Complete Experimental Data	27
Appendix B Cross Section Showing PZT Expansion Directions	31
Appendix C Comparison with a MEMS Fabrication T-beam	33

LIST OF FIGURES

Figure 2.1: T-beam concept: (a) as fabricated, and deflected shapes with a clamped left end and voltage is applied between (b) web and bottom electrode, (c) between flanges and bottom electrode, (d) left flange and bottom electrode, and (e) right flange and bottom electrode.....	3
Figure 3.1: T-beam model: (a) the initial and deflected shape and (b) cross section	5
Figure 3.2: Fabricated T-beam Device 1 ($t_1 = 167.8 \mu\text{m}$), Device 2 ($t_2 = 324.3 \mu\text{m}$), Device 3 ($t_3 = 523.5 \mu\text{m}$), Device 4 ($t_4 = 719.3 \mu\text{m}$).....	7
Figure 3.3: Packaged device with chrome/gold web/bottom electrodes and silver painted right and left flange electrodes.....	9
Figure 3.4: Back view of the packaged beam showing the 4 electrodes and the mount.	10
Figure 4.1: Virtual tip deflection test.....	11
Figure 4.2: T-beam test cases. $V =$ positive applied voltage, Solid arrow = motion direction, Dashed arrow = polarization direction, $ $ = floating electrode. Arrows inside structure indicate electric field. Maximum voltage is shown below each case.	14
Figure 4.3: Device 1 upward out-of-plane actuation. Experimental results: $\blacklozenge =$ Case 1, $\bullet =$ Case 2, $\blacktriangle =$ Case 3, $\blacksquare =$ Case 4.....	15
Best fit lines: Solid = Case 1, Dashed = Case 2, Dotted = Case 3, Dash-Dot = Case 4.....	15
Figure 4.4: Device 2 upward out-of-plane actuation. Experimental results: $\blacklozenge =$ Case 1, $\bullet =$ Case 2, $\blacktriangle =$ Case 3, $\blacksquare =$ Case 4.....	15
Best fit lines: Solid = Case 1, Dashed = Case 2, Dotted = Case 3, Dash-Dot = Case 4.....	15
Figure 4.5: Device 3 upward out-of-plane actuation. Experimental results: $\blacklozenge =$ Case 1, $\bullet =$ Case 2, $\blacktriangle =$ Case 3, $\blacksquare =$ Case 4.....	16
Best fit lines: Solid = Case 1, Dashed = Case 2, Dotted = Case 3, Dash-Dot = Case 4.....	16
Figure 4.6: Device 4 upward out-of-plane actuation. Experimental results: $\blacklozenge =$ Case 1, $\bullet =$ Case 2, $\blacktriangle =$ Case 3, $\blacksquare =$ Case 4.....	16

Best fit lines: Solid = Case 1, Dashed = Case 2, Dotted = Case 3, Dash-Dot = Case 4.....	16
Figure 4.7: Device 1 downward out-of-plane actuation.	17
Experimental Results: ● = Case 5, ▲ = Case 6, ■ = Case 7.	17
Best fit lines: Solid = Case 5, Dashed = Case 6, Dotted = Case 7.....	17
Figure 4.8: Device 2 downward out-of-plane actuation.	18
Experimental Results: ● = Case 5, ▲ = Case 6, ■ = Case 7.	18
Best fit lines: Solid = Case 5, Dashed = Case 6, Dotted = Case 7.....	18
Figure 4.9: Device 3 downward out-of-plane actuation.	18
Experimental Results: ● = Case 5, ▲ = Case 6, ■ = Case 7.	18
Best fit lines: Solid = Case 5, Dashed = Case 6, Dotted = Case 7.....	18
Figure 4.10: Device 4 downward out-of-plane actuation.	19
Experimental Results: ● = Case 5, ▲ = Case 6, ■ = Case 7.	19
Best fit lines: Solid = Case 5, Dashed = Case 6, Dotted = Case 7.....	19
Figure 4.11: In-plane actuation. Symbol: ◆ = Device 1, ● = Device 2, ▲ = Device 3, ■ = Device 4. Open = left actuation (Case 8), Filled = right actuation (Case 9).	20
Best fit lines: Solid = Device 1, Dashed = Device 2, Dotted = Device 3, Dash-Dot = Device 4.....	20
Figure 2.1: Cross-sectional view of PZT under applied voltages.....	31
Figure 2.2: Polarization vs. Electric Field hysteresis curve for 100μm thick PZT.....	32
Figure 3.1: T-beam MEMS fabrication process	33
Figure 3.2: Photograph of the fabricated and mounted T-beam actuator with web and underside electrodes.....	34
Figure 3.3: Experimental actuator tip displacement w(L) vs. web voltage (V).....	35
Figure 3.4: Experimental actuator tip displacement w(L) vs. field (V/μm). Best fit slope value = 8.273 μm/(V/μm).	36

LIST OF TABLES

Table 3.1: Parameters for the T-beam actuator.....	8
Table 4.1: Device parameters (b=0.7 mm and s = 4.4 mm for all devices).....	12
Table 4.2: Displacement vs. field slope values ($\mu\text{m}/(\text{V}/\mu\text{m})$) for all devices and cases.....	20
Table 1.1: Device 1 displacement data	27
Table 1.2: Device 2 displacement data	28
Table 1.3: Device 3 displacement data	29
Table 1.4: Device 4 displacement data	30

ACKNOWLEDGEMENTS

I would like to thank Dr. Chris Rahn for guiding me through my Master's research and for inspiring me to be the kind of professor he is. I would also like to thank Dr. Srinivas Tadigadapa for advising my fabrication efforts and for pushing me beyond what I thought I was capable of.

I would also like to thank my labmates, Kiron Mateti, Ashish Patwardhan, Nicholas Duarte, Prasoon Joshi, Ping Kao, Bharadwaja Srowthi, and Siddharth Sonti for all their wisdom and for making my graduate experience enjoyable.

I would also like to thank the National Science Foundation and the GREATT Program for funding my graduate education and for instilling a love of teaching. The students and teachers of Park Forest Middle School, Nittany Valley Charter School, Our Lady Victory, and the Danville Correctional Facility will always be in my heart.

I would like to thank my family and friends for their love and encouragement. I would not have made it without you. And thanks God for allowing me the opportunity to show love and serve the people of State College during my graduate career.

Chapter 1

Introduction

Piezoelectric actuators are used for many applications, including precision-positioning stages, ultra-fine focusing in optical equipment, and structural vibration sensing and control. Piezoelectric ceramic actuators have desirable properties such as high energy density, high bandwidth, and high force actuation. Most piezoelectric actuators use lead zirconate titanate (PZT) as opposed to quartz or barium titanate due to the greater electro-mechanical coupling coefficients and piezoelectric constants. However, PZT exhibits a maximum strain of only ~0.1% and large motion is not possible without strain amplification. Larger motion has been realized with stack actuators [1, 2, 3] which stack layers of PZT alternatively poled through the thickness connected to the positive and negative terminals of a high voltage source. This interdigitated setup allows the poling direction, electric field, and displacement to be in the same direction. The stack actuator design takes advantage of the d_{33} piezoelectric constant which is larger than the d_{31} constant (~ 1/3 of d_{33}) used in unimorph or bimorph configurations. A unimorph actuator has an active PZT layer poled through the thickness bonded to a passive elastic layer [3, 4, 5, 6]. The active layer expands through the thickness and contracts along the length to produce out-of-plane bending motion due to the offset between the neutral axis and the center of the active layer due to the passive layer. A bimorph actuator replaces the passive layer with another active layer and allows for maximum transverse displacement because each layer can be activated with the

maximum field in the direction of poling. The field opposite the poling direction is limited to $\sim 1/3$ the maximum field in the direction of poling so that the PZT will not depole. PZT and PZN-PT based unimorph actuators have been fabricated and shown to produce large out-of-plane motion for use in a micromechanical flapping mechanism [11]. In-plane strain-amplifying piezoelectric actuators have been demonstrated with low voltage/low displacement [12, 13, 14]. A serpentine-style design [15, 16] has been developed to amplify the displacement for unimorph and bimorph actuators.

At the microscale, stack and unimorph/bimorph actuators are difficult to fabricate. Although solder bonding techniques for PZT have been shown [7], stack actuators of more than a few layers have not been fabricated. Unimorph actuators have been made [4, 8] using low performance ZnO and AlN. Thin film PZT has also been used in these actuators but lacks the quality of bulk PZT [9] and stress mismatch between the layers during fabrication results in variably deformed structures upon release. Tube actuators that can produce bimorph actuation in two directions have been demonstrated at the 1-10 mm scale [10].

This thesis describes a new type of monolithic actuator fabricated from bulk PZT using a high precision dicing saw. Using this method, a T-shaped two-axis bimorph actuator can be machined and experimentally shown to produce both out-of-plane and in-plane motion. Optimal application of voltage to the T-beam electrodes is developed that maximizes displacement.

Chapter 2

T-Beam Concept

The T-beam actuator can provide bimorph actuation in two directions as shown in Figure 2.1. The T-beam actuator is cantilevered and has a T-shaped cross section. The entire T-beam is bulk PZT with electrodes deposited on the top of the web, the top of each flange, and the bottom of the flange. The PZT is poled through the thickness from top to bottom.

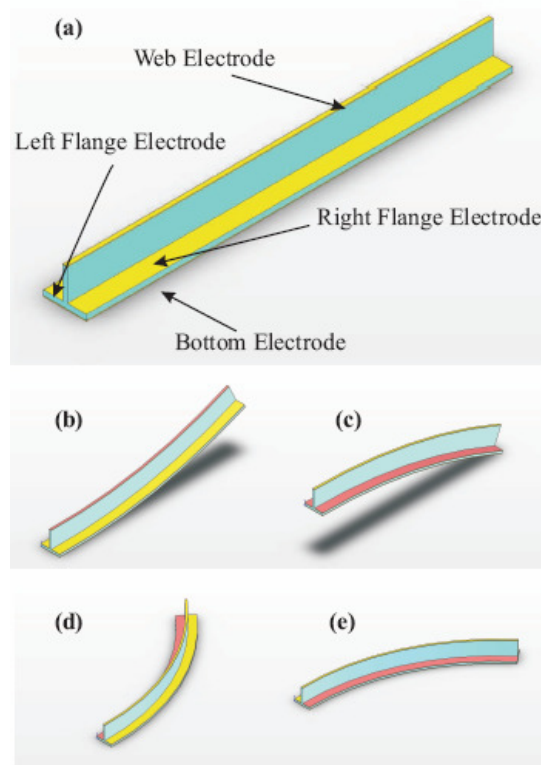


Figure 2.1: T-beam concept: (a) as fabricated, and deflected shapes with a clamped left end and voltage is applied between (b) web and bottom electrode, (c) between flanges and bottom electrode, (d) left flange and bottom electrode, and (e) right flange and bottom electrode.

Figure 2.1 shows how the T-beam actuator can be bent both in-plane and out-of-plane by selectively activating the electrodes. The web or flange sections can either expand or contract longitudinally through the d_{31} piezoelectric effect. The active part of the structure (web/flange) either expands or contracts longitudinally while the passive part (flange/web, respectively) acts to constrain the T-beam and effectively creates a unimorph actuator. Out-of-plane upward displacement can be achieved by applying a field that either contracts the web section only (unimorph), expands the two flanges only (unimorph), or both (bimorph) to further increase displacement (see Figure 2.1(b)). Out-of-plane downward displacement can be achieved either by expanding the web section only (unimorph), contracting the two flanges only (unimorph), or both (bimorph) (see Figure 2.1(c)).

It is desirable to activate the structure at its maximum electric field, E_{MAX} , in the direction of poling. The maximum field opposite the direction of poling, however, is typically limited to $1/3 E_{MAX}$ so as not to depole the structure. Hence, the bimorph T-beam design with maximum field applied for both upward and downward motion provides much larger displacement than with a single active layer (unimorph).

The T-beam can also provide in-plane displacement by differential application of voltage on the two flanges. To bend left as shown in Figure 2.1(d), the left flange electrode is actuated at E_{MAX} and the right flange electrode can either be passive and provide unimorph actuation or active at $-1/3 E_{MAX}$. To bend right, the left and right flange electrode fields are switched (see Figure 2.1(e)).

Chapter 3

Actuator Design & Device Fabrication

3.1 Actuator Design

The T-beam model developed by Kommepalli et al. [11] show that the T-beam geometry can be optimized to produce maximum displacement. Figure 3.1 shows the cross section used in the modeling with controllable fabrication parameters flange width s , flange thickness t , web thickness b , and (fixed) overall thickness h .

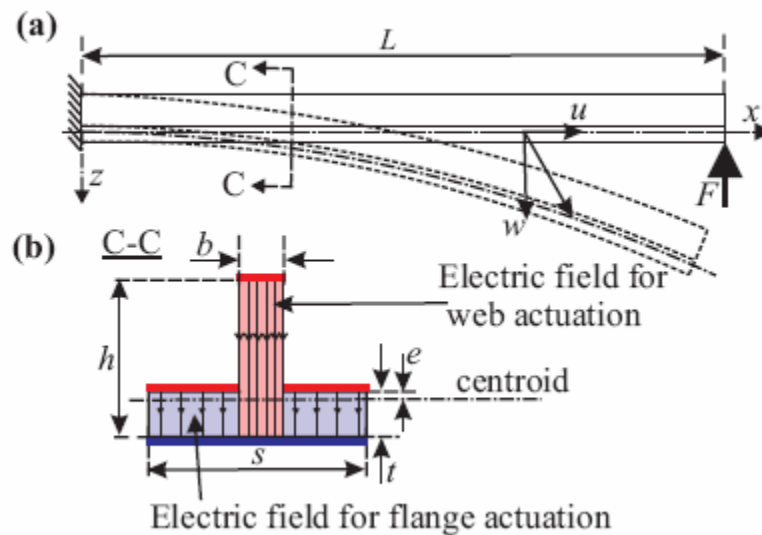


Figure 3.1: T-beam model: (a) the initial and deflected shape and (b) cross section

The T-beam is modeled as a cantilever beam using Euler-Bernoulli beam theory. Voltage is applied between the web (V_w) or the two flange electrodes (V_G) and bottom electrode. V_w and V_G are assumed to produce uniform uni-axial electric fields only in

the web and flange sections, respectively. Equation 3.1 gives the tip displacement equation.

$$w(L) = - \frac{L^2 (2FL + 3a_{4M} A_p)}{6 (EI_{be} + 2a_2 I_{pe} + 2a_{3M} A_p)} \quad (\text{Equation 3.1})$$

Noting that $M = W, G$ for web and flange actuation, respectively allows the following parameters and values from Table 3.1 to be substituted into Equation 3.1:

$$\begin{aligned} A_p &= bh \\ I_{be} &= \frac{1}{3} t (t^2 + 3e^2 - 3et) (s - b) \\ e &= \frac{1}{2} \frac{t^2 s - t^2 b + 2tbh - bh^2}{ts - tb + bh} \\ I_{pe} &= \frac{bh^3}{12} + bh \left(\frac{h}{2} - t + e \right)^2 \\ a_2 &= \frac{1}{2} \left(E + \frac{e_{31}^2}{\epsilon_{33}} \right) \\ e_{31} &= Ed_{31} \\ a_{3W} &= - \frac{e_{31}^2 (2e + h - 2t)^2}{8\epsilon_{33}} \\ a_{4W} &= - \frac{e_{31} V_W (2e + h - 2t)}{2h} \\ a_{3G} &= - \frac{e_{31}^2 (2e - t)^2}{8\epsilon_{33}} \\ a_{4G} &= - \frac{e_{31} V_G (2e - t)}{2t} \end{aligned} \quad (\text{Equation 3.2})$$

3.2 Device Fabrication

The T-beam actuators are fabricated using a Kulicke & Soffa Industries Model 980 precision dicing saw. T-beams with different parameters (t , s , b) can quickly be fabricated and tested because they are simple to dice from bulk PZT (Boston Piezo Optics (BPO) Navy Type I, PZT-4) and electrode. The process starts with 1" x 1" x 1 mm bulk PZT with chrome/gold electrodes on both sides and poled through the thickness. The chip is mounted on a 4" Si wafer using 1827 photoresist for stability during machining. Four devices with different flange thicknesses, t_1 , t_2 , t_3 , t_4 are machined with the same flange width, $s = 4.4$ mm, and web width, $b = 0.7$ mm. Cutting speed is set to 0.3 mm/s and the saw is programmed to take overlapping cuts with the 275 μm wide blade in order to machine smooth flanges. The varying flange thicknesses on the mounted devices can be seen in Figure 3.2. Table 3.1 shows all the parameters for the fabricated T-beam actuators.

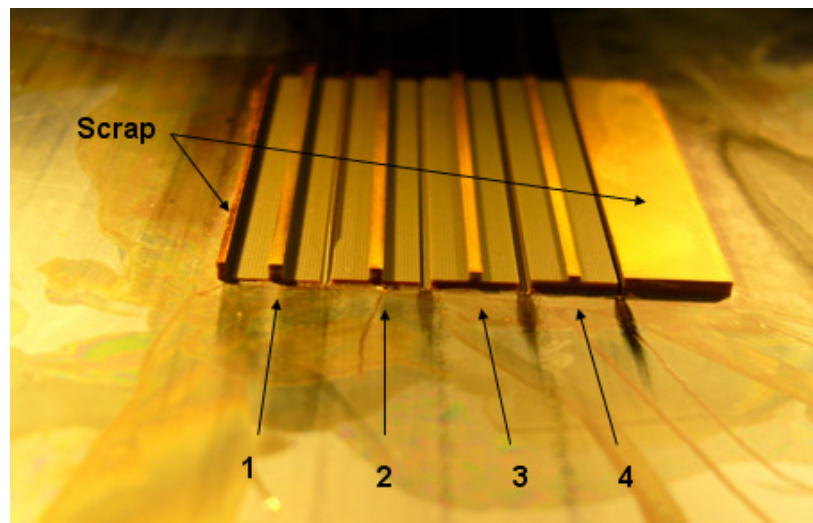


Figure 3.2: Fabricated T-beam Device 1 ($t_1 = 167.8 \mu\text{m}$), Device 2 ($t_2 = 324.3 \mu\text{m}$), Device 3 ($t_3 = 523.5 \mu\text{m}$), Device 4 ($t_4 = 719.3 \mu\text{m}$)

Table 3.1: Parameters for the T-beam actuator

Youngs Modulus of PZT, E (GPa)	78
Flange thickness, t (μm)	t_1, t_2, t_3, t_4
Web width, b (mm)	0.7
Flange width, s (mm)	4.4
Actuator thickness, h (μm)	1000
Actuator length, L (mm)	≈ 19.0
Piezoelectric strain coeff. d_{31} (C/N)	-122e-12
Permittivity of PZT, ϵ_{33} (C^2/Nm^2)	1.15105e-08

The beams are released and cleaned in acetone/IPA before packaging. All devices have a chrome/gold bottom and web electrode. The flange electrodes are applied using a needle and colloidal silver liquid from Electron Microscopy Sciences and then cured at low temperature. Significant efforts were made to keep excess paint from sticking to the sides of the web and flanges. After the electrodes are deposited, the beams are mounted to a 24 PIN package using silver epoxy and super glue to provide the clamped boundary condition. To prevent PZT poling degradation that takes place at high temperature, the beams are cured in an oven at $\sim 45^\circ\text{C}$ for 8 hours. The web, bottom, left flange, and right flange electrode are then wire bonded to a pin on the package. The 24 PIN package is solder bonded to a larger circuit board that allows for easy positioning during testing. Figure 3.3 shows a schematic of the final packaged device.

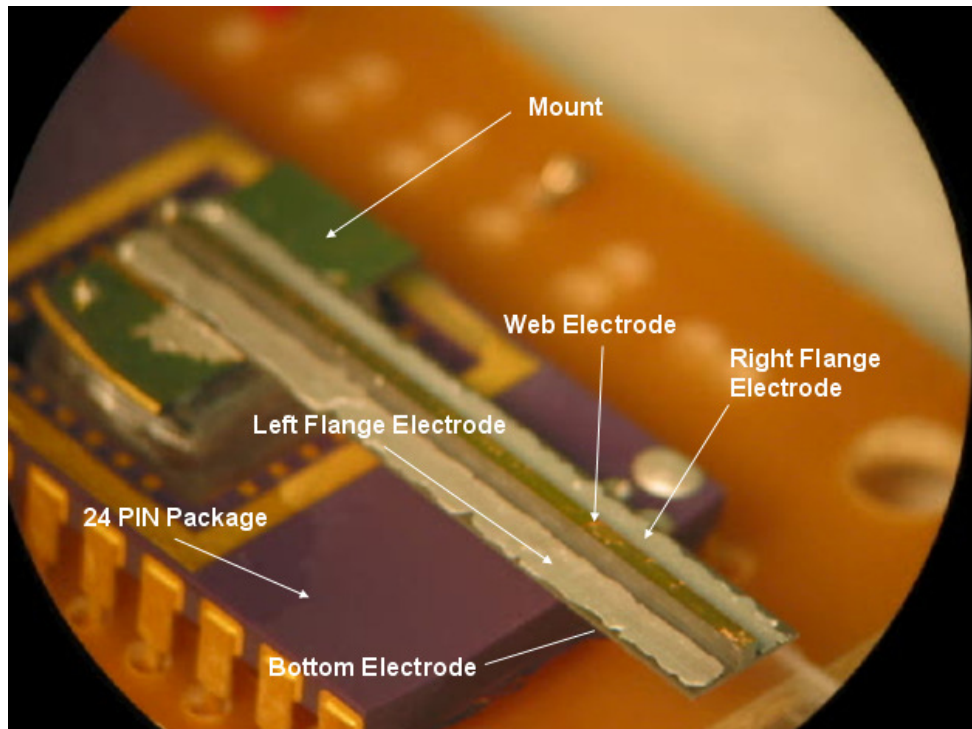


Figure 3.3: Packaged device with chrome/gold web/bottom electrodes and silver painted right and left flange electrodes.

Figure 3.4 shows how the base of the beam is mounted to the package and wire bonded. The underside of the beam is gold electroded so the silver epoxy electrically connects the bottom electrode to the gold coated mount in the package. In addition to being joined with silver epoxy, the beam is super-glued onto the mount to provide the clamped boundary condition.

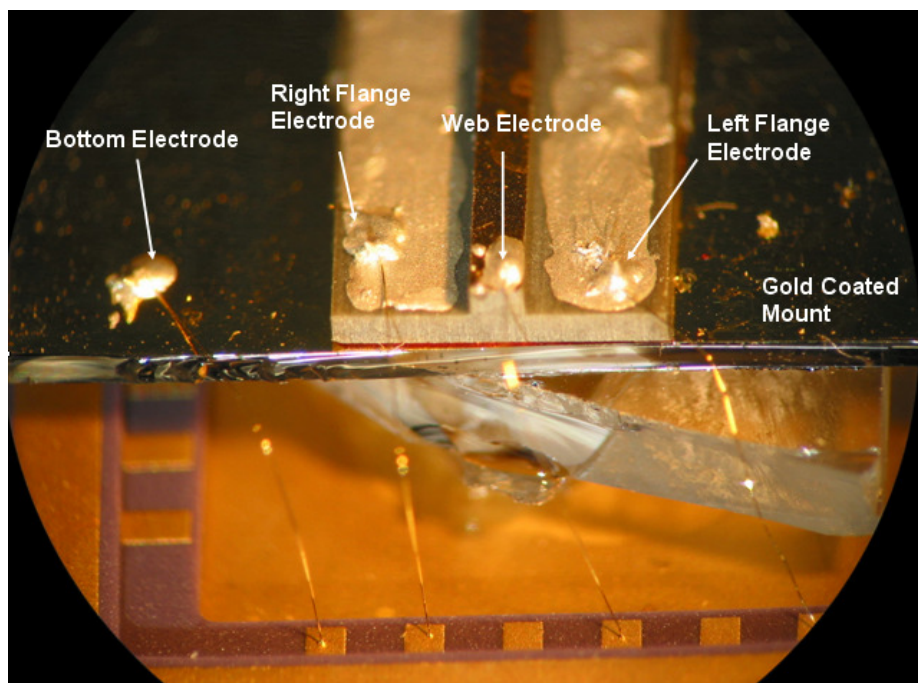


Figure 3.4: Back view of the packaged beam showing the 4 electrodes and the mount.

Chapter 4

Experimental Setup and Testing

4.1 Experimental Setup

Tip displacement for the four devices was measured at several voltages applied to the four electrodes. Tests were conducted using a Hirox MX-5030RZ microscope (500x magnification) with a Sony High Resolution CCD-Iris color video camera and television screen. Transparencies were placed on the television screen and a fine-tipped Sharpie marker was used to mark the origin and subsequent beam displacements. Microscopic imperfections in the PZT made convenient places to mark displacement. The DC voltage was applied, the new position marked, the voltage switched off, and the power supply shorted to return the beam to the zero position. Figure 4.1 shows an example tip deflection test. A Vernier caliper was used to take measurements between markings.

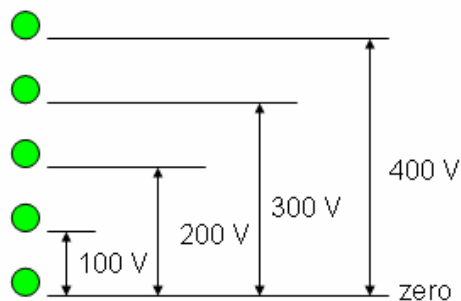


Figure 4.1: Virtual tip deflection test.

A calibration factor was used to convert physical transparency measurements to actual micrometer beam tip displacements. The thickness of a glass slide was used as the calibration standard and measured to be $151\mu\text{m}$ with a micrometer with $1\mu\text{m}$ precision. The glass slide measured 90.0 mm on the screen transparency so the scale factor of $151\mu\text{m}/90.0\text{mm}$ was used.

This testing method produced repeatable measurements with small error. The largest source of error was the diameter of the pen markings which were approximately 0.5mm . Converted to displacement measurements, the measurement uncertainty is less than a micron.

4.2 Device Characteristics

Table 4.1: Device parameters ($b=0.7\text{ mm}$ and $s = 4.4\text{ mm}$ for all devices)

Device	$t\ (\mu\text{m})$	$L\ (\text{mm})$
1	167.8	18.98
2	324.3	18.84
3	523.5	19.34
4	719.3	14.51

Each beam length was measured from the cantilevered end to the free end with a Vernier caliper (See Table 4.1). In order to make a fair comparison between cantilevered beams, length was normalized to 19.0 mm using a correction formula based on the L^2 relationship given by the final displacement equation in Equation 3.1. The nominal measured tip displacement can be found from Equation 4.1.

$$w_{\text{meas}} \left(\frac{L_{\text{nominal}}}{L_{\text{actual}}} \right)^2 = w_{\text{meas}}^{\text{nominal}} \quad (\text{Equation 4.1})$$

4.3 Device Testing

This study seeks to find the combinations of +V, ground, and float applied to the four electrodes that maximizes out-of-plane and in-plane displacement. Although it is possible to provide large field in the direction of poling, the actuator displacement saturates and significant field increases do not yield increased displacement. It was observed on a test device that ~550V ($E = 0.55\text{V}/\mu\text{m}$) applied between the bottom and web electrode ($h = 1\text{ mm}$) opposite the direction of poling was enough to depole the material. In this study, the field is calculated as the applied voltage divided by the minimum separation between the electrodes. An arbitrary low field, $E_{\text{MAX}} = 0.4\text{ V}/\mu\text{m}$, is used to ensure that the material does not depole or arcs do not occur between electrodes.

The voltage application cases are shown in Figure 4.2. The desired direction of motion, polarization direction, electric field, and maximum applied voltage are shown. Cases 1-4 yield upward out-of-plane displacement, Cases 5-7 yield downward out-of-plane displacement, and Cases 8-9 yield in-plane displacement. The maximum voltages are geometry dependent, and hence, device dependent. In addition to limiting the field in the polarization direction, the field opposite the direction of poling is maintained to be less than $1/3 E_{\text{MAX}}$. In Cases 3 and 7, the applied voltage depends on the flange thickness to ensure that the field is neither too great in the web nor the flange.

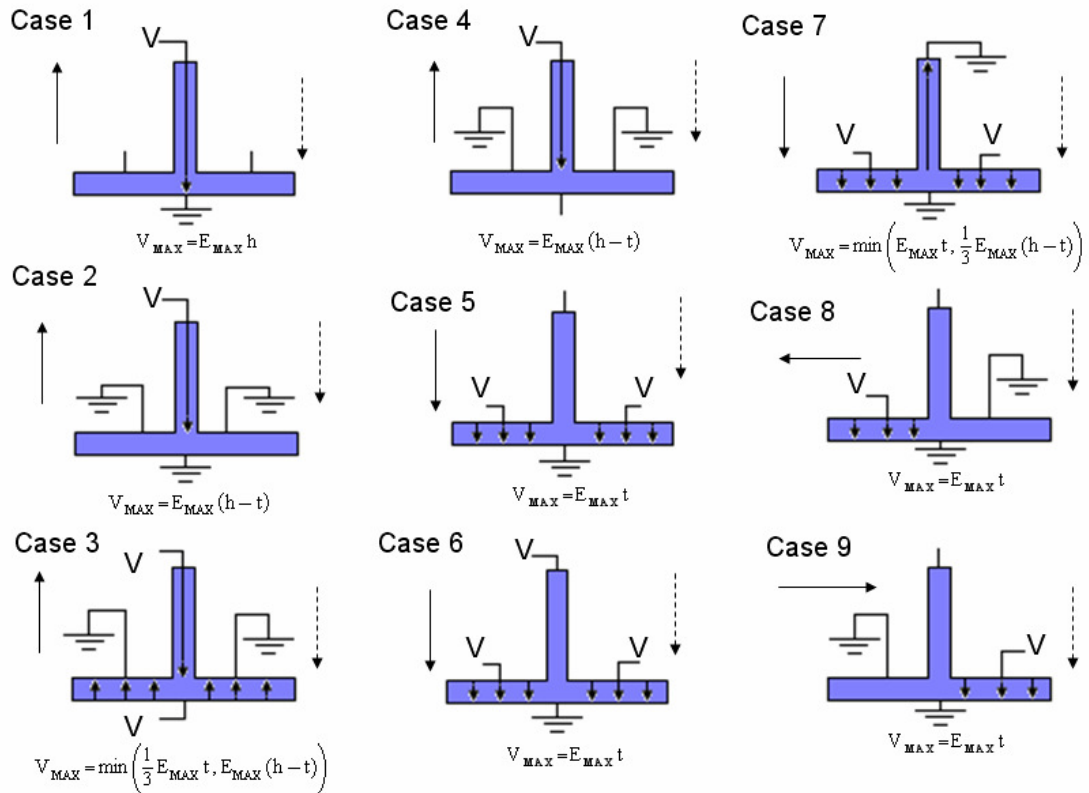


Figure 4.2: T-beam test cases. V = positive applied voltage, Solid arrow = motion direction, Dashed arrow = polarization direction, \square = floating electrode. Arrows inside structure indicate electric field. Maximum voltage is shown below each case.

Four cases yield upward displacement (1, 2, 3, 4). Figure 4.3 – Figure 4.6 graphs the tip displacement, $w(L)$ versus field for these cases and Device 1-4, respectively. Each point represents an experimentally measured displacement and a best-fit linear regression is fitted to the data points. The slopes of the best fit lines for all 9 cases and 4 devices are shown in Table 4.2.

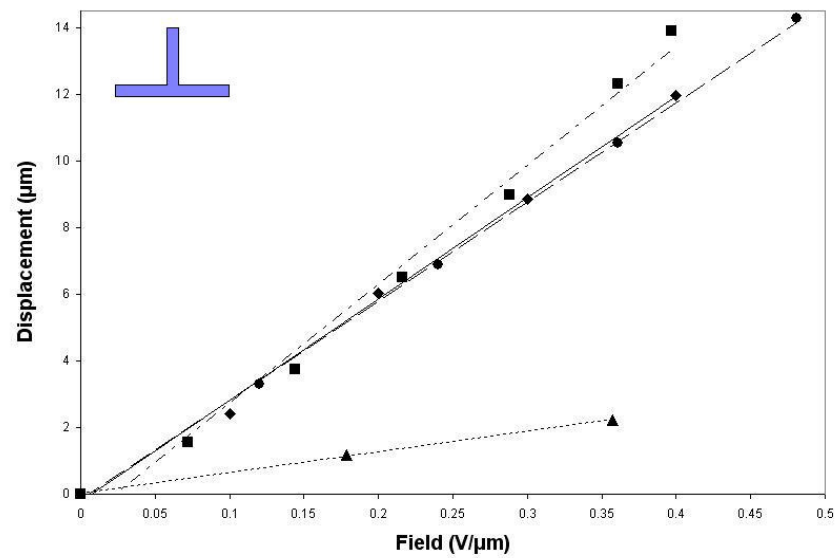


Figure 4.3: Device 1 upward out-of-plane actuation. Experimental results: \blacklozenge = Case 1, \bullet = Case 2, \blacktriangle = Case 3, \blacksquare = Case 4.

Best fit lines: Solid = Case 1, Dashed = Case 2, Dotted = Case 3, Dash-Dot = Case 4

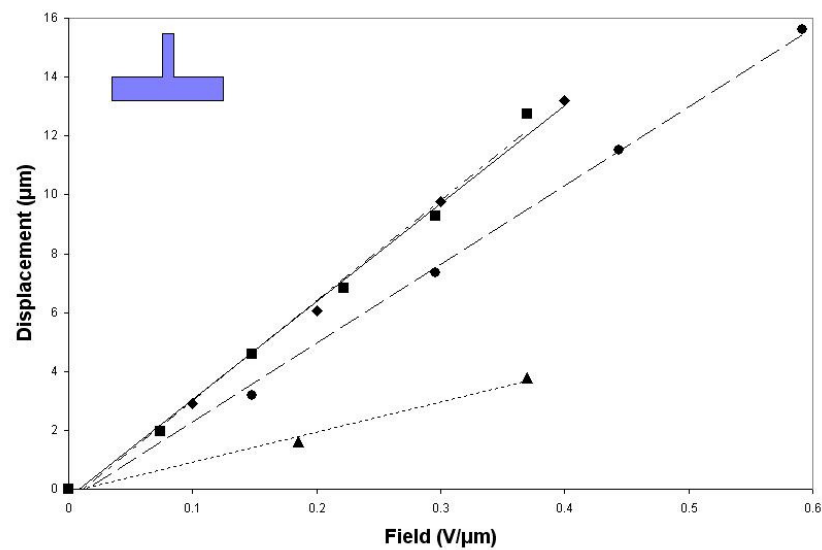


Figure 4.4: Device 2 upward out-of-plane actuation. Experimental results: \blacklozenge = Case 1, \bullet = Case 2, \blacktriangle = Case 3, \blacksquare = Case 4.

Best fit lines: Solid = Case 1, Dashed = Case 2, Dotted = Case 3, Dash-Dot = Case 4

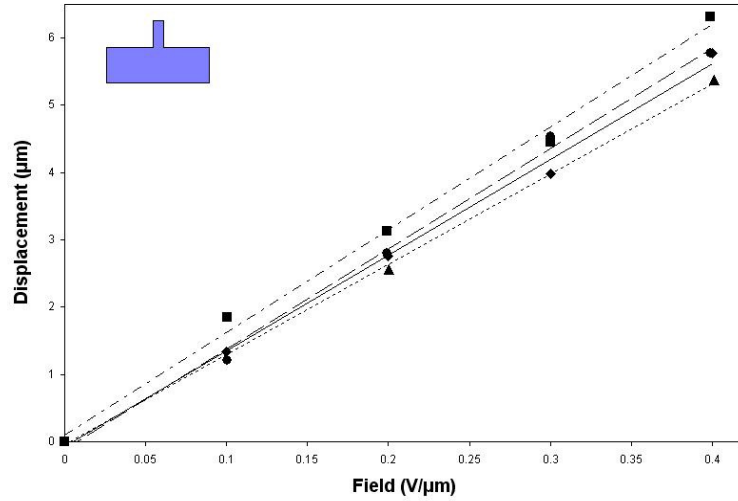


Figure 4.5: Device 3 upward out-of-plane actuation. Experimental results: \blacklozenge = Case 1, \bullet = Case 2, \blacktriangle = Case 3, \blacksquare = Case 4.

Best fit lines: Solid = Case 1, Dashed = Case 2, Dotted = Case 3, Dash-Dot = Case 4

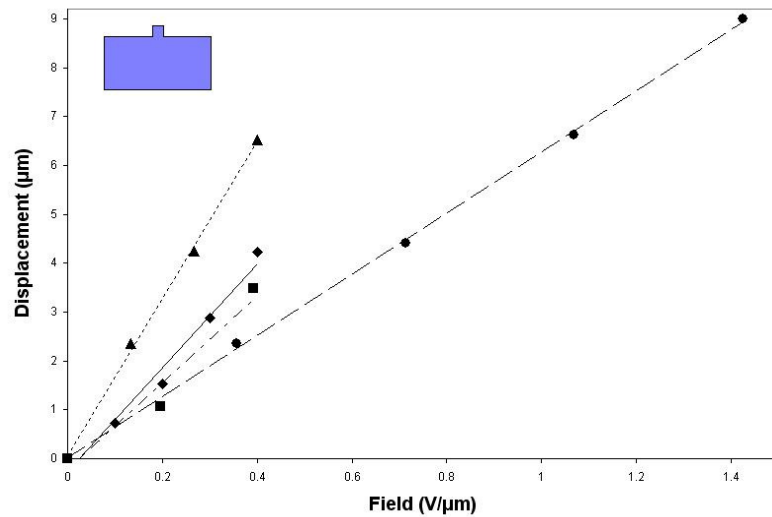


Figure 4.6: Device 4 upward out-of-plane actuation. Experimental results: \blacklozenge = Case 1, \bullet = Case 2, \blacktriangle = Case 3, \blacksquare = Case 4.

Best fit lines: Solid = Case 1, Dashed = Case 2, Dotted = Case 3, Dash-Dot = Case 4

Cases 5, 6, and 7 produce downward out-of-plane displacement. Figure 4.7 – Figure 4.10 shows the experimental results and best-fit regression lines for the cases in Devices 1-4, respectively.

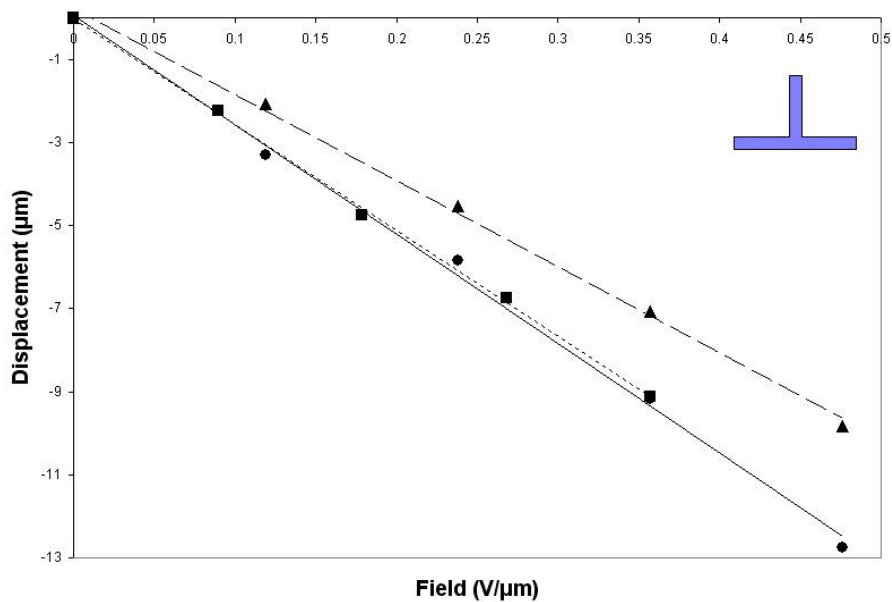


Figure 4.7: Device 1 downward out-of-plane actuation.

Experimental Results: ● = Case 5, ▲ = Case 6, ■ = Case 7.

Best fit lines: Solid = Case 5, Dashed = Case 6, Dotted = Case 7.

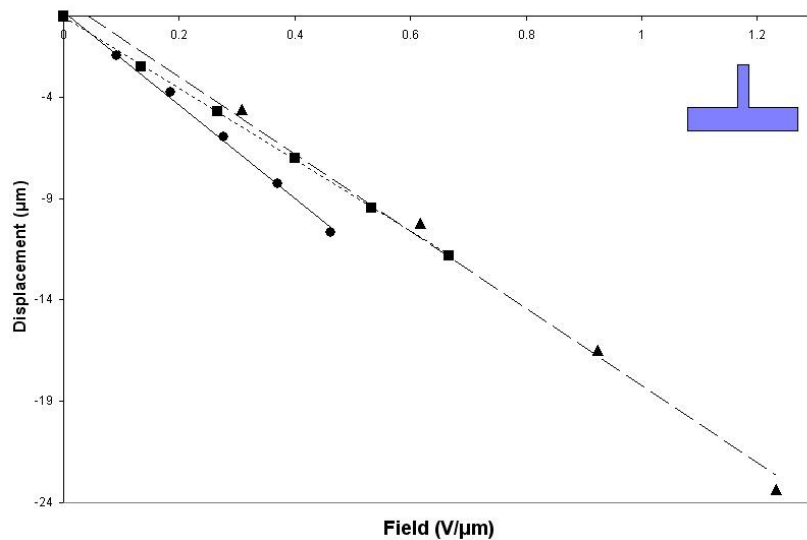


Figure 4.8: Device 2 downward out-of-plane actuation.

Experimental Results: ● = Case 5, ▲ = Case 6, ■ = Case 7.

Best fit lines: Solid = Case 5, Dashed = Case 6, Dotted = Case 7.

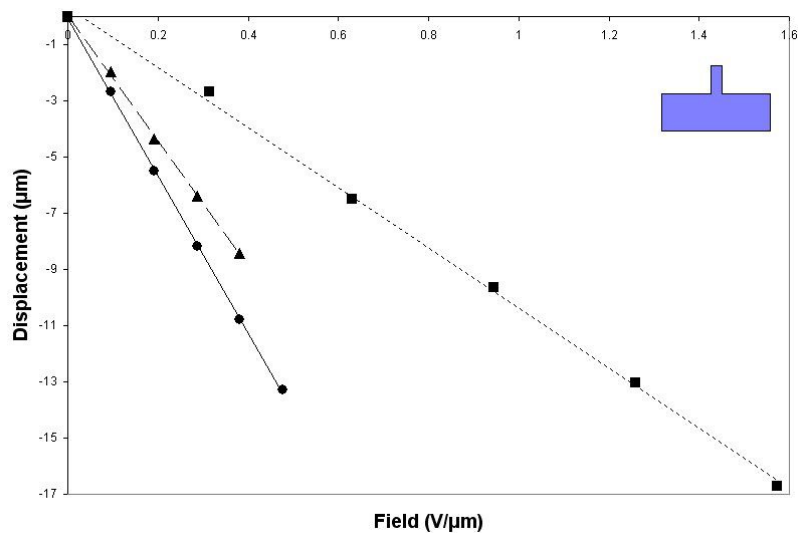


Figure 4.9: Device 3 downward out-of-plane actuation.

Experimental Results: ● = Case 5, ▲ = Case 6, ■ = Case 7.

Best fit lines: Solid = Case 5, Dashed = Case 6, Dotted = Case 7.

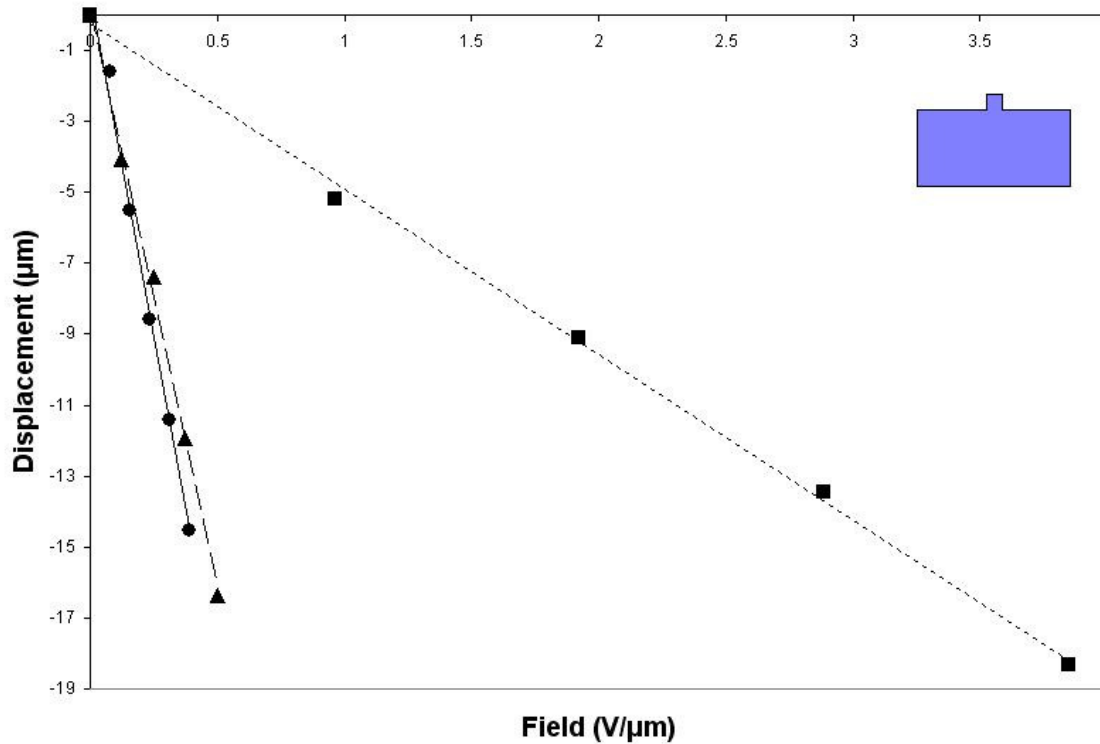


Figure 4.10: Device 4 downward out-of-plane actuation.

Experimental Results: ● = Case 5, ▲ = Case 6, ■ = Case 7.

Best fit lines: Solid = Case 5, Dashed = Case 6, Dotted = Case 7.

Figure 4.11 shows the tip displacement versus field graphs for the in-plane displacement Cases 8 and 9. In these graphs the absolute values of the left and right deflection are plotted versus the applied field.

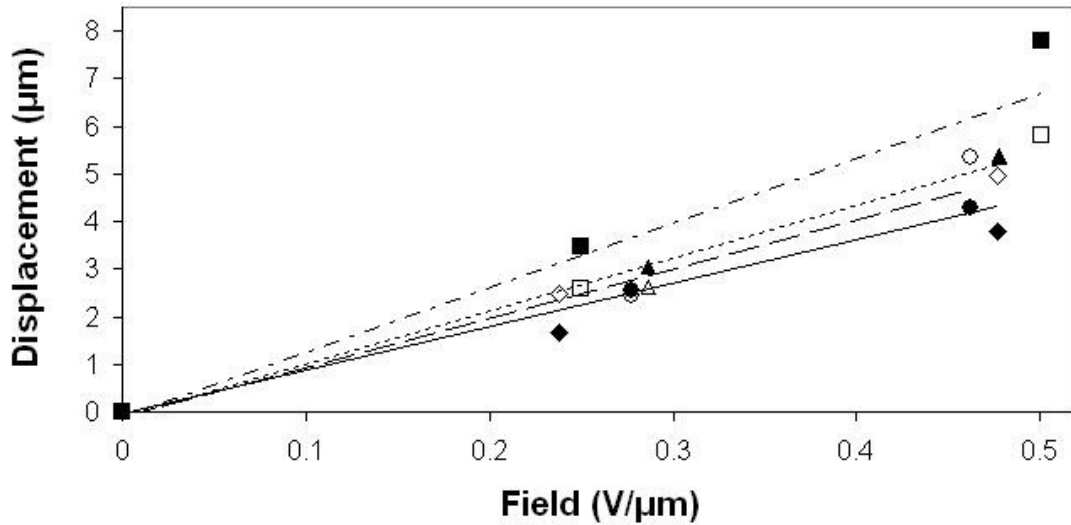


Figure 4.11: In-plane actuation. Symbol: \blacklozenge = Device 1, \bullet = Device 2, \blacktriangle = Device 3, \blacksquare = Device 4. Open = left actuation (Case 8), Filled = right actuation (Case 9).

Best fit lines: Solid = Device 1, Dashed = Device 2, Dotted = Device 3, Dash-Dot = Device 4

Table 4.2: Displacement vs. field slope values ($\mu\text{m}/(\text{V}/\mu\text{m})$) for all devices and cases

Case		1	2	3	4
Out-of-Plane Upward	1	30.348	33.258	14.201	10.615
	2	29.768	26.738	14.928	6.250
	3	6.214	10.238	13.402	16.101
	4	35.642	33.938	15.286	8.883
Out-of-Plane Downward	5	-26.339	-23.042	-27.960	-38.619
	6	-20.733	-18.981	-22.261	-32.442
	7	-25.516	-17.628	-10.691	-4.669
In-Plane	8 & 9	9.169	10.310	11.134	13.594
MEMS T-beam = 8.273					

4.4 Results and Discussion

The experimental results show excellent linearity for the applied fields. In some cases, the field exceeds the desired $0.4 \text{ V}/\mu\text{m}$ (reaching $4 \text{ V}/\mu\text{m}$ for Device 4 and Case 7 in Figure 4.7(d)) but the experimental displacement stays close to the best fit line. This indicates that the applied field could be increased by as much as an order of magnitude without detrimental effects (See Figure 4.7(d)). The excellent linearity means that the best-fit line slopes are a useful metric to determine the best actuation schemes. The best-fit line slopes for all devices and cases are summarized in Table 4.2.

Device 1 and Case 4 provided the largest upward out-of-plane displacement. This device had the thinnest flange and Case 4 provided voltage to the top of the web, ground on the top of the two flanges, and float on the bottom electrode. Cases 1 and 2 were close to Case 4 for all devices and Case 3 performed poorly for the thin flanged devices but had the highest displacement for the thick flanged Device 4. It is anticipated, however, that if two levels of voltage ($E_{\text{MAX}}*(h-t)$ on the web and $E_{\text{MAX}}*t/3$ on the bottom electrode) could be applied in Case 3 then the performance would increase and may outperform all other cases for all devices. With the same voltage on both the flange and web, it was limited by the maximum field in the thinnest dimension. The applied voltage on the web was much lower in Case 3 for the thin flanged devices because it was limited to $E_{\text{MAX}}*t/3$. Although Cases 1, 2, and 4 had very similar voltage application schemes, they produced different displacements. This is due to the complex interaction between the applied voltage, electrostatic field, induced strain, and geometry in the T-beam actuators.

Device 4 and Case 5 produced the largest downward out-of-plane displacement. In this case, voltage was applied to the top of the flange, the bottom electrode was grounded, and the web electrode floated. It is interesting to note that Case 7 in the thin flanged Device 1 did not produce more displacement than Case 5 and 6. The web was reverse biased, presumably leading to larger out-of-plane displacement than Cases 5 and 6. Again, the choice of floating or ground electrodes led to significantly different performance due to the complex electromechanics of the T-beam actuator.

The maximum in-plane displacement occurred in Device 4. This device has the thickest flange and hence more active material relative to the passive web. The best-fit linear regression is fitted to both left and right actuation (4 data points). The differences in right and left deflection arise from slightly different right and left flange widths during fabrication.

Chapter 5

Conclusions & Future Work

This thesis shows that T-beam actuators demonstrate bimorph actuation in two directions using a monolithic PZT structure. The T-beam actuators are fabricated using simple dicing and electrode application. Selective application of voltage, float, and ground to the four T-beam electrodes creates bending upward, downward, left, and right. Applied voltage limits are postulated based on the maximum allowable field in the PZT and minimum distances between the electrodes. The T-beam devices exhibit linear displacement for applied voltages up to $0.4 \text{ V}/\mu\text{m}$. The slopes of the displacement versus field best-fit lines are used to compare voltage application schemes. It is found that thinner flanges produce more out-of-plane displacement and thicker flanges produce more in-plane displacement. Reverse-biasing the inactive material was not found to improve displacement.

T-beam actuators suffer from the same limitations as bi-morph actuators. Long and thin beams are needed to produce large displacements. The fabricated T-beam devices, having actuator lengths of $\sim 19\text{mm}$, provided displacements of only $\sim 10\text{-}20\mu\text{m}$ using upwards of 400V . For comparison, a $100\mu\text{m}$ thick MEMS fabricated T-beam (See Appendix C and Figure 3.3), at only 8mm long, provided $21\mu\text{m}$ displacement at 270V , despite having a low slope value in Table 4.2. Thus, using MEMS fabrication and thin PZT has the potential to provide large displacements at low voltages.

Future work will continue to develop designs taking advantage of MEMS fabrication. Testing the devices at higher field will also be necessary to maximize actuator performance. Retesting these four devices and measuring the induced voltage on the floating electrode would also be of interest. Modeling of the electromechanics of T-beams has the potential to explain the counter-intuitive results observed in the experiments.

Bibliography

1. Giurgiutiu, V., and Rogers, C.A., 1996. "Energy based comparison of solid state induced strain actuators". *Journal of Intelligent Material Systems and Structures*, **7**, January, pp. 4-14.
2. Giurgiutiu, V., Rogers, C.A., and Chaudhry, Z., 1997. "Design of displacement amplified induced-strain actuators for maximum energy output". *Journal of Mechanical Design*, **119**, December, pp. 511-517.
3. Uchino, K., 2003. *Micromechatronics*. Marcel Dekker, New York.
4. Percin, G., 2001. "Micromachined piezoelectrically actuated flextensional transducers for high resolution printing and imaging". *IEEE Ultrasonics Symposium*, pp. 921-924.
5. Basak, S., Raman, A., and Garimella, S. V., 2005. "Dynamic response optimization of piezoelectrically excited thin resonant beams". *Journal of Vibration and Acoustics*, **127**, pp. 18-27.
6. Wang, Q.-M., Du, X.-H., Xu, B., and Cross, L. E., 1999. "Electromechanical coupling and output efficiency of piezoelectric bending actuators". *IEEE Transactions on Ultrasonics, Ferroelectrics, and Frequency Control*, **46**(3), pp. 638-646.
7. Goyal, A., Cheong, J., and Tadigadapa, S. A., 2004. "Tin-based solder bonding for mems fabrication and packaging applications". *Journal of Micromechanics and Microengineering*, **14**(6), June, pp. 819-825.
8. Cheong, J., Tadigadapa, S. A., and Rahn, C. D., 2005. "Fabrication and performance of a flextensional microactuator". *Journal of Micromechanics and Microengineering*, **15**, pp. 1947-1955.
9. Gross, S. J., Tadigadapa, S. A., Jackson, T. N., Trolier-McKinstry, S., and Zhang, Q. Q., 2003. "Lead-zirconate-titanate based piezoelectric micromachined switch". *Applied Physics Letters*, **83**(1), July, pp. 174-176.
10. Berg, M., Hagedorn, P., and Gutschmidt, S., 2004. "On the dynamics of piezoelectric cylindrical shells". *Journal of Sound and Vibration*, **274**(1-2), July, pp. 91-109.

11. Kommepalli, H. K. R., Hirsh, A. D., Rahn, C. D., and Tadigadapa, S. A., 2008. "Piezoelectric T-beam microactuators". *Proceedings of ASME International Design Engineering Technical Conferences*, August, pp. 1-6.
12. Sitti, M., Campolo, D., Yan, J., Fearing, R. S., Su, T., Taylor, D., and Sands, T., 2001. "Development of PZT and PZN-PT based unimorph actuators for micromechanical flapping mechanisms". *IEEE Conference on Robotics and Automation*, May, pp. 3839-3846.
13. Conway, N. J., Traina, Z. J., and Kim, S.-G., 2007. "A strain amplifying piezoelectric MEMS actuator". *Journal of Micromechanics and Microengineering*, **17**(2007), March, pp. 781-787.
14. Lee, T.-M., Seo, Y. H., Whang, K.-H., and Choi, D.-S., 2006. "Study on the lateral piezoelectric actuator with actuation range amplifying structure". *Trans Tech Publications, Switzerland*, December, pp. 1-4.
15. Seo, Y. H., Choi, D.-S., Lee, J.-H., Je, T.-J., and Whang, K.-H., 2005. "Laterally driven thin film PZT actuator with high-aspect-ratio silicon beam for stroke amplification". *Sensors and Actuators A*, **127**(2006), November, pp. 302-309.
16. Fang, H., Liu, L., and Ren, T., 2006. "Modeling and design optimization of large-deflection piezoelectric folded cantilever microactuators". *IEEE Transactions on Ultrasonics, Ferroelectrics, and Frequency Control*, **53**(1), January, pp. 237-240.

Appendix A

Complete Experimental Data

This section includes the experimental data used for Figure 4.3 - Figure 4.11.

Table 1.1: Device 1 displacement data

Case	Voltage (V)	Field (V/ μm)	w(L)_meas_nom (μm)
1	0	0	0
1	100	0.1	2.404281203
1	200	0.2	6.03592274
1	300	0.3	8.843719669
1	400	0.4	11.95415339
2	0	0	0
2	100	0.120192308	3.312191587
2	200	0.240384615	6.893393658
2	300	0.360576923	10.54184835
2	400	0.480769231	14.27436882
3	0	0	0
3	10	0.178571429	1.176920869
3	20	0.357142857	2.219336495
4	0	0	0
4	60	0.072115385	1.56362344
4	120	0.144230769	3.749333624
4	180	0.216346154	6.489877932
4	240	0.288461538	8.995038067
4	300	0.360576923	12.30722965
4	330	0.396634615	13.88766625
5	0	0	0
5	20	0.119047619	-3.295378432
5	40	0.238095238	-5.834164877
5	60	0.357142857	-9.163169619
5	80	0.476190476	-12.74437169
6	0	0	0
6	20	0.119047619	-2.068018098
6	40	0.238095238	-4.539551921
6	60	0.357142857	-7.078338366
6	80	0.476190476	-9.83569583
7	0	0	0
7	15	0.089285714	-2.23614965
7	30	0.178571429	-4.75812294
7	45	0.267857143	-6.758888416
7	60	0.357142857	-9.129543309
8	0	0	0
8	40	0.238379023	2.471533824
8	80	0.476758045	4.959880803
9	0	0	0
9	40	0.238379023	1.681315526
9	80	0.476758045	3.782959935

Table 1.2: Device 2 displacement data

Case	Voltage (V)	Field (V/ μm)	w(L)_meas_nom (μm)
1	0	0	0
1	100	0.1	2.900873323
1	200	0.2	6.040642097
1	300	0.3	9.777649495
1	400	0.4	13.19044164
2	0	0	0
2	100	0.14799467	3.173896695
2	200	0.29598934	7.354567072
2	300	0.44398402	11.51817349
2	400	0.59197869	15.61352406
3	0	0	0
3	20	0.18501388	1.604012308
3	40	0.37002775	3.788199281
4	0	0	0
4	50	0.07399734	1.962355483
4	100	0.14799467	4.590205435
4	150	0.22199201	6.842648251
4	200	0.29598934	9.265730673
4	250	0.36998668	12.74677866
5	0	0	0
5	30	0.09250694	-1.945291523
5	60	0.18501388	-3.77113532
5	90	0.27752081	-5.972386254
5	120	0.37002775	-8.276020951
5	150	0.46253469	-10.68203941
6	0	0	0
6	100	0.30835646	-4.590205435
6	200	0.61671292	-10.23837643
6	300	0.92506938	-16.4667221
6	400	1.23342584	-23.32643431
7	0	0	0
7	30	0.1331952	-2.508402227
7	60	0.26639041	-4.726717121
7	90	0.39958561	-7.030351819
7	120	0.53278082	-9.453434241
7	150	0.66597602	-11.80826082
8	0	0	0
8	90	0.27752081	2.457210344
8	150	0.46253469	5.341019707
9	0	0	0
9	90	0.27752081	2.542530148
9	150	0.46253469	4.300118103

Table 1.3: Device 3 displacement data

Case	Voltage (V)	Field (V/ μm)	w(L)_meas_nom (μm)
1	0	0	0
1	100	0.1	1.344023284
1	200	0.2	2.752818775
1	300	0.3	3.983490698
1	400	0.4	5.780919428
2	0	0	0
2	48	0.10073452	1.214478871
2	95	0.19937041	2.80139793
2	143	0.30010493	4.534054453
2	190	0.39874082	5.780919428
3	0	0	0
3	35	0.20057307	2.558502156
3	70	0.40114613	5.376093137
4	0	0	0
4	48	0.10073452	1.846007884
4	95	0.19937041	3.125258962
4	143	0.30010493	4.453089195
4	190	0.39874082	6.315290131
5	0	0	0
5	50	0.09551098	-2.671853517
5	100	0.19102197	-5.489444499
5	150	0.28653295	-8.177491067
5	200	0.38204394	-10.80076543
5	250	0.47755492	-13.27830233
6	0	0	0
6	50	0.09551098	-1.975552297
6	100	0.19102197	-4.339737834
6	150	0.28653295	-6.396255389
6	200	0.38204394	-8.420386841
7	0	0	0
7	50	0.31479538	-2.688046569
7	100	0.62959077	-6.493413699
7	150	0.94438615	-9.651058764
7	200	1.25918153	-13.0192135
7	250	1.57397692	-16.72742232
8	0	0	0
8	150	0.28653295	2.607081311
8	250	0.47755492	5.376093137
9	0	0	0
9	150	0.28653295	3.060486756
9	250	0.47755492	5.359900086

Table 1.4: Device 4 displacement data

Case	Voltage (V)	Field (V/ μm)	w(L)_meas_nom (μm)
1	0	0	0
1	100	0.1	0.719195272
1	200	0.2	1.524693976
1	300	0.3	2.876781087
1	400	0.4	4.228868198
2	0	0	0
2	100	0.35625223	2.358960492
2	200	0.71250445	4.401475063
2	300	1.06875668	6.616596501
2	400	1.42500891	9.004324803
3	0	0	0
3	32	0.13346309	2.358960492
3	64	0.26692618	4.257636009
3	96	0.40038927	6.530293068
4	0	0	0
4	55	0.19593872	1.064409002
4	110	0.39187745	3.480905116
5	0	0	0
5	56	0.07785347	-1.582229598
5	112	0.15570694	-5.523419687
5	168	0.23356041	-8.601575451
5	224	0.31141387	-11.42082092
5	280	0.38926734	-14.52774449
6	0	0	0
6	90	0.12512165	-4.085029144
6	180	0.25024329	-7.364559583
6	270	0.37536494	-11.93864151
6	360	0.50048658	-16.36888439
7	0	0	0
7	90	0.96188101	-5.206973768
7	180	1.92376202	-9.090628236
7	270	2.88564304	-13.46333549
7	360	3.84752405	-18.32509553
8	0	0	0
8	180	0.25024329	2.589102978
8	360	0.50048658	5.811097796
9	0	0	0
9	180	0.25024329	3.480905116
9	360	0.50048658	7.796076746

Appendix B

Cross Section Showing PZT Expansion Directions

The following figure shows expansion and contraction directions under specified polarity and applied electric field directions.

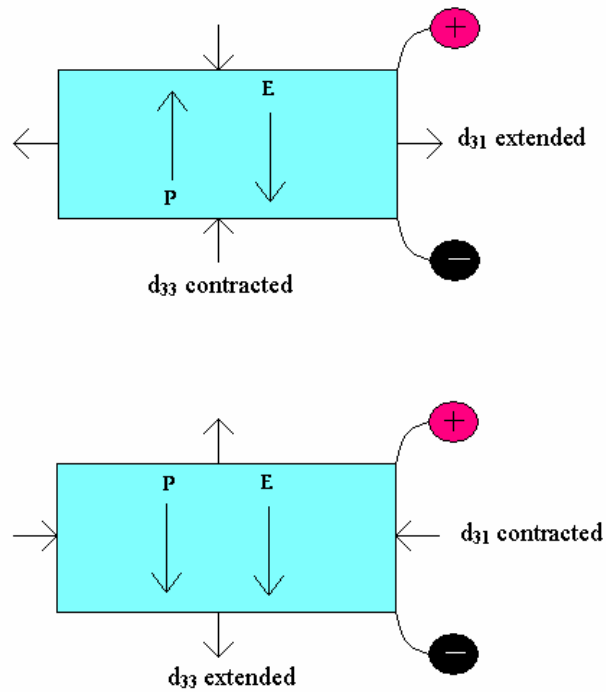


Figure 2.1: Cross-sectional view of PZT under applied voltages

Also for reference in Figure 2.2 is a hysteresis diagram for a 100 μm BPO Navy-I PZT-4 sample. Although 10 times thinner than the bulk PZT used in this thesis, it is roughly the same material and will give an estimate for the coercive field, E_c . Material can vary slightly depending on the PZT supplier for BPO. Testing was done courtesy of Bharadwaja Srowthi in the Penn State Materials Research Institute.

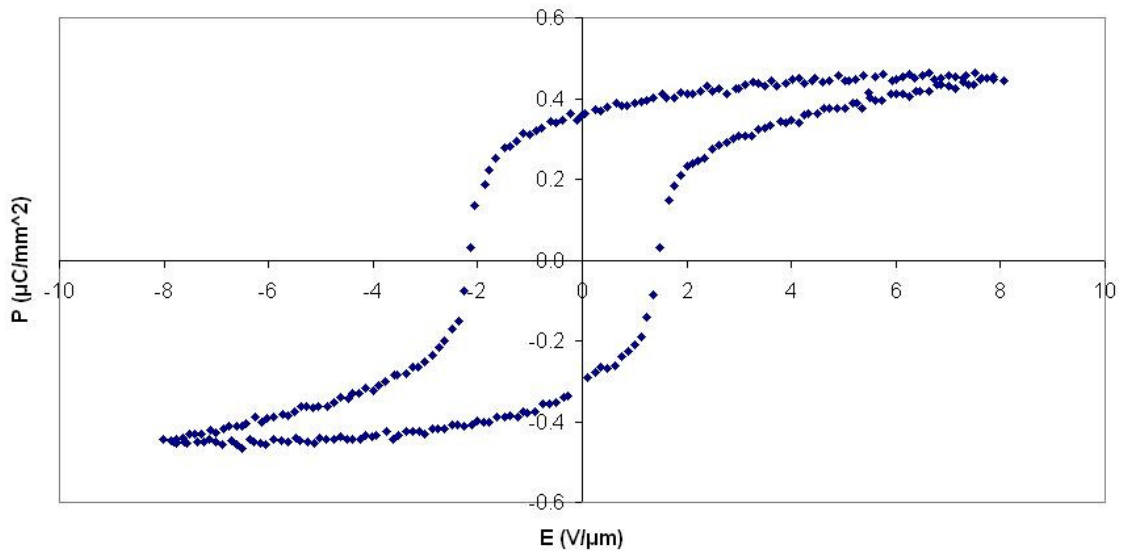


Figure 2.2: Polarization vs. Electric Field hysteresis curve for 100µm thick PZT

The coercive field, the X value where the curve crosses the +X-axis is found to be $E_C \approx 1.44 \text{ V}/\mu\text{m}$. Taking half that as electrical energy input gives $0.72 \text{ V}/\mu\text{m}$. The voltage that depoled a T-beam with only web and underside electrodes was 550 V. The field here is $550\text{V}/1000\mu\text{m} \approx 0.55 \text{ V}/\mu\text{m}$. This value serves as an estimate as to when the 1mm thick PZT would experience polarization reversal.

Appendix C

Comparison with a MEMS Fabrication T-beam

This section highlights another T-beam utilizing a successful MEMS fabrication process. The MEMS fabrication process can be seen in Figure 3.1.

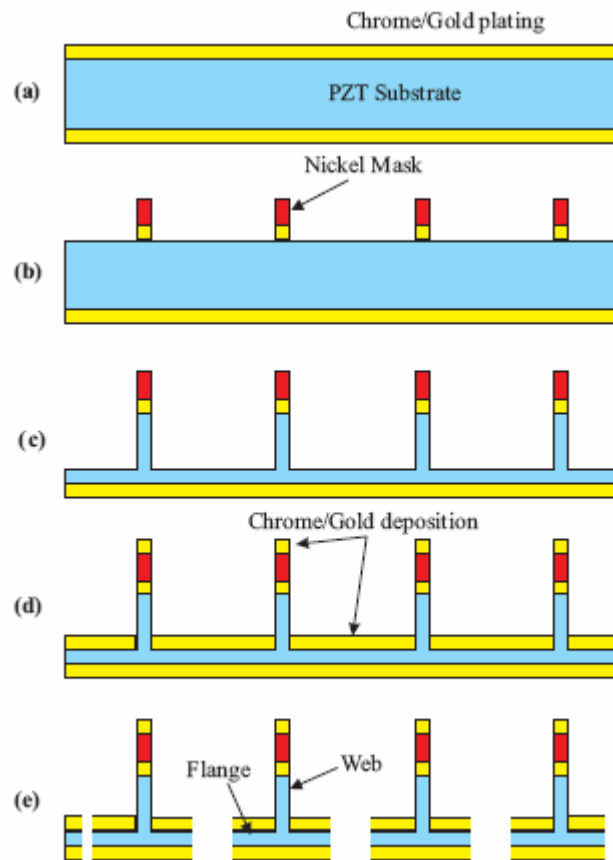


Figure 3.1: T-beam MEMS fabrication process

Figure 3.1(a) shows the stock 1"x1"x 100 μm thick bulk PZT coated with 500 \AA chrome and 2000 \AA gold and lap polishing from the Boston Piezo Optics. The PZT is then

aligned and patterned leaving only the web electroded with chrome/gold. This web electrode is then electroplated in a nickel solution with 18-22 μm Ni which acts as a hard mask as shown in Figure 3.1(b). Figure 3.1(c) shows the results of the hour-long ICP-RIE etch process. A maximum etch rate of 19-25 $\mu\text{m/hr}$ of PZT is obtained using 2000 W of ICP power, 475 W of substrate power, 5 sccm of sulfur hexafluoride (SF_6), and 50 sccm of argon (Ar) on the PZT substrate. The T-beams are then released using a dicing saw. Figure 3.1(c,d) show additional fabrication steps to deposit flange electrodes, which were not included in the first experimental device. Figure 3.2 shows the final packaged MEMS device.

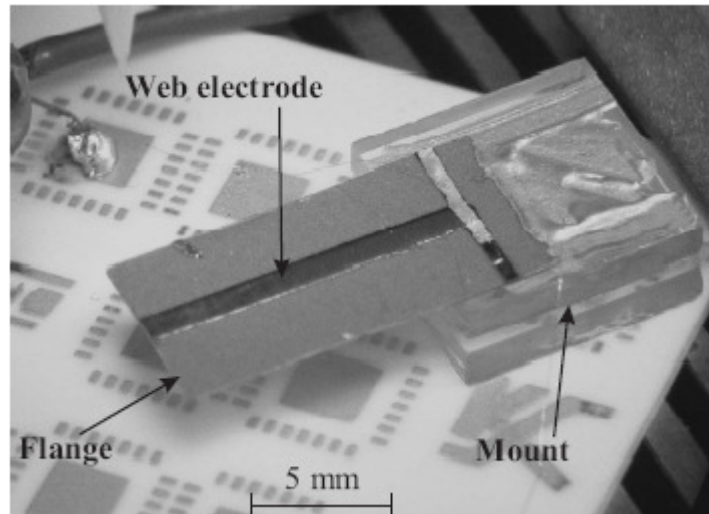


Figure 3.2: Photograph of the fabricated and mounted T-beam actuator with web and underside electrodes.

This T-beam was first created to test the feasibility of design and has no flange electrodes and therefore is only capable of web actuated out-of-plane actuation. The PZT was

etched to a depth of $17\mu\text{m}$. Dimensions for the T-beam are flange thickness $t = 83\mu\text{m}$, web width $b = 1\text{mm}$, actuator thickness $h = 100\mu\text{m}$, flange width $s = 6\text{mm}$, and actuator length $L = 8\text{mm}$.

The displacement of the T-beam actuator is measured using a laser vibrometer as a function of applied voltage. Figure 3.3 shows the experimental displacement (\blacktriangle) versus applied voltage up to 270 V. The 8 mm long actuator produces a maximum displacement of $21.52\mu\text{m}$ as shown in Figure 3.3.

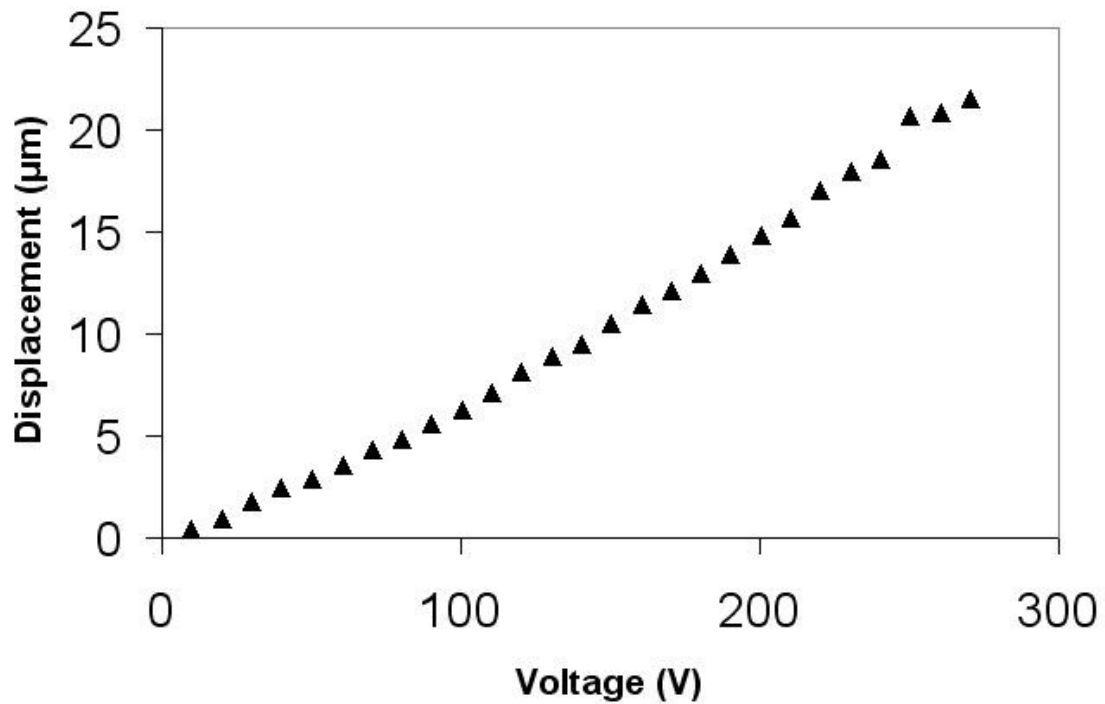


Figure 3.3: Experimental actuator tip displacement $w(L)$ vs. web voltage (V)

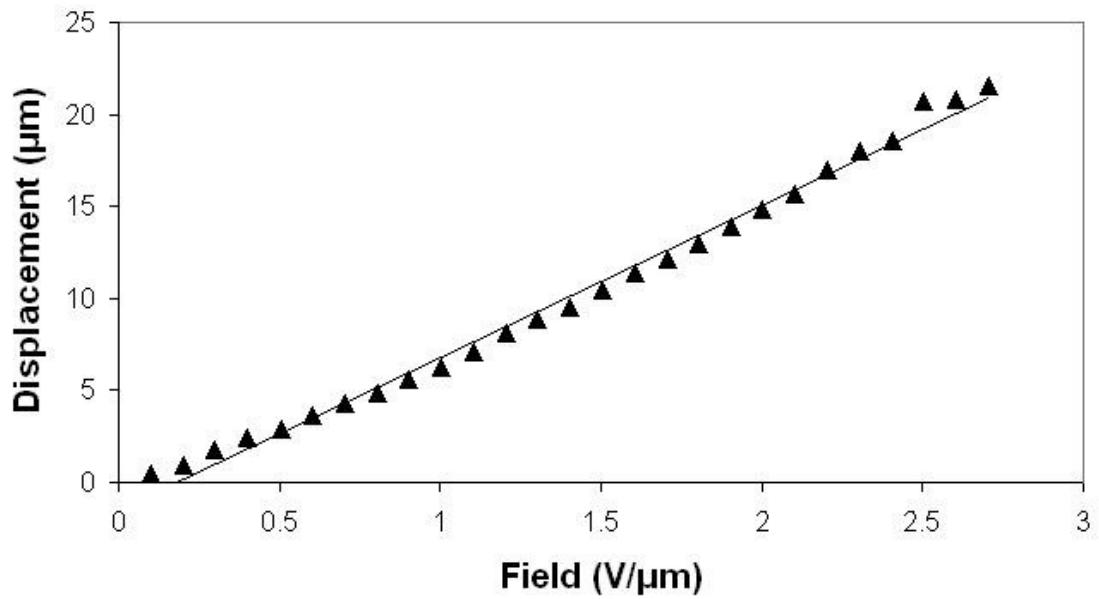


Figure 3.4: Experimental actuator tip displacement $w(L)$ vs. field ($V/\mu\text{m}$). Best fit slope value = $8.273 \mu\text{m}/(V/\mu\text{m})$.
